Single particle cryo-EM structure of the outer hair cell motor protein prestin

Carmen Butan [1,*], Qiang Song [1,*], Jun-Ping Bai, Winston J. T. Tan [1], Dhasakumar Navaratnam [1, 2, 3], Joseph Santos-Sacchi [1, 2, 4]

[1] Surgery (Otolaryngology), [2] Neuroscience, [3] Neurology and [4] Cellular and Molecular Physiology, Yale University School of Medicine, 333 Cedar Street, New Haven, CT 06510, USA

[*]Contributed equally to this work.

CB carried out the cryo-EM experiments: grid freezing, single particle-data collection, data processing and structure determination and wrote the manuscript.

QS designed experiments, expressed and purified proteins and performed mutagenesis.

JP and WT designed experiments and performed electrophysiological experiments and analysis.

DSN and JSS designed experiments, analyzed data and wrote the manuscript.

Running title: prestin structure reveals OHC electromotility mechanism

Acknowledgements: This research was supported by NIH-NIDCD R01 DC016318 (JSS) and R01 DC008130 (JSS, DN).

Keywords: Prestin (Slc26a5), Cryo-EM, cochlear amplification, NonLinear Capacitance

Corresponding authors:

Joseph Santos-Sacchi
Surgery (Otolaryngology), Neuroscience, and Cellular and Molecular Physiology
Yale University School of Medicine
333 Cedar Street
New Haven, CT 06510
e-mail: joseph.santos-sacchi@yale.edu

Dhasakumar Navaratnam
Neurology, Neuroscience, and Surgery (Otolaryngology)
Yale University School of Medicine
333 Cedar Street
New Haven, CT 06510
e-mail: dhasakumar.navaratnam@yale.edu

Abstract

The mammalian outer hair cell (OHC) protein prestin (Slc26a5), a member of the solute carrier 26 (Slc26) family of membrane proteins, differs from other members of the family owing to its unique piezoelectric-like property that drives OHC electromotility. Prestin is required by OHCs for cochlear amplification, a process that enhances mammalian hearing. Despite substantial biophysical characterization, the mechanistic basis for the prestin's electro-mechanical behavior is not fully understood. To gain insight into such behavior, we have used cryo-electron microscopy at subnanometer resolution (overall resolution of 4.0 Å) to investigate the three-dimensional structure of prestin from *gerbil* (*Meriones unguiculatus*). Our studies show that prestin dimerizes with a 3D architecture strikingly similar to the dimeric conformation observed in the Slc26a9 anion transporter in an inside open/intermediate state, which we infer, based on patch clamp recordings, to reflect the contracted state of prestin. The structure shows two well separated transmembrane (TM) subunits and two cytoplasmic sulfate transporter and anti-sigma factor antagonist (STAS) domains forming a swapped dimer. The dimerization interface is defined by interactions between the domain-swapped STAS dimer and the transmembrane domains of the opposing half unit, further strengthened by an antiparallel beta strand at its N terminus. The structure also shows that each one of its two transmembrane subunits consists of 14 transmembrane segments organized in two inverted 7-segment repeats with a topology that was first observed in the structure of bacterial symporter UraA (Lu F, et al., Nature 472, 2011). Finally, the solved anion binding site structural features of prestin are quite similar to that of Slc26a9 and other family members. Despite this similarity, we find that Slc26a9 lacks the characteristic displacement currents (or **N**on**L**inear **C**apacitance(NLC)) found with prestin, and we show that mutation of prestin's Cl^- binding site removes salicylate competition with anions in the face of normal **NLC**, thus refuting the yet accepted extrinsic voltage sensor hypothesis and any associated transport-like requirements for voltage-driven electromotility.

Introduction

The outer hair cell (OHC) molecular motor prestin (Slc26a5) belongs to a diverse family of transporters that includes Slc26, Slc4 and Slc23 (Chang and Geertsma, 2017). Unlike other members of these families, and unique to membrane proteins, prestin functions as a voltage driven motor with exceedingly rapid kinetics, likely providing cycle by cycle amplification of sound within the mammalian organ of Corti (Santos-Sacchi et al., 2006; Dallos et al., 2008; Santos-Sacchi and Tan, 2020). The underlying basis of prestin's electromechanical capabilities resides in its unique piezoelectric-like property that drives OHC electromotility (Iwasa, 1993; Gale and Ashmore, 1994; Kakehata and Santos-Sacchi, 1995; Ludwig et al., 2001; Santos-Sacchi et al., 2001). For members of this diverse family, known structures are dimers with each protomer showing a common 7+7 inverted repeat topology containing a core and gate domain; these proteins function variably as ion channels and transporters with a range of substrates (Chang and Geertsma, 2017; Yu et al., 2017; Chang et al., 2019). Within the Slc26 family, prestin and pendrin (Slc26a4) are unique in showing voltage sensitivity with signature **N**on**L**inear **C**apacitance (NLC) or equivalently, displacement currents/gating charge movements (Ashmore, 1990; Santos-Sacchi, 1991; Kuwabara et al., 2018); while pendrin lacks intrinsic electromechanical behavior (Tang et al., 2011), prestin is a minimal transporter (Ashmore, 2005; Bai et al., 2009b). With more structural information there have been competing visions of transporter mechanisms (elevator vs. rocker) (Drew and Boudker, 2016; Ficici et al., 2017), although how these fit with prestin's electromechanical behavior remains speculative at best. To be sure, the lack of structural information for full-length prestin has precluded an understanding of its unique molecular motor function. In this study, we have used single particle cryo-electron microscopy to determine the structure of prestin from gerbil (*Meriones unguiculatus*) at sub-nanometer resolution that confirms Oliver's initial modelling efforts (Gorbunov et al., 2014), and, remarkably, bears high concordance with the recently determined cryo-EM structures of Slc26a9 (Walter et al., 2019; Chi et al., 2020). Prestin forms a dimer and the cryo-EM density map has allowed us to build a nearly complete model of the protein. In combination with electrophysiological data, our results suggest that the inward cytosol facing conformation we find is that of prestin in the contracted

state. Furthermore, mutations within prestin's now structurally confirmed anion binding site show that the extrinsic voltage sensor hypothesis (Oliver et al., 2001) is likely incorrect (Santos-Sacchi et al., 2017), with the wider implication that a transporter-like mechanism driving electromotility is unlikely.

Results

Cryo-EM structure of full-length Slc26a5

We used single particle cryo-electron microscopy to obtain the structure of detergent solubilized prestin from gerbil (*Meriones unguiculatus*). The protein, extracted and purified in the presence of digitonin/GDN (synthetic digitonin substitute glyco-diosgenin), appears to be a homogeneous oligomer when assessed with size-exclusion chromatography (**Supplementary Figure 1A**).

The cryo-EM images obtained from plunge-frozen specimens of solubilized prestin (**Figure 1A**) revealed clear density for the transmembrane helices (TM), the cytoplasmic domains and the micelle surrounding the protein (**Figure 1B**). An electron-density map (**Figure 1C**) was obtained at an overall resolution of 4.0 Å according to the gold-standard Fourier shell correlation (FSC) from 122,754 particles with C2 symmetry (**Supplementary Figure 2B**). This map has enabled us to see densities visible for many of the bulky side chains and to build a nearly complete model of full-length prestin (**Figure 1D**). Prestin oligomerizes as a dimer. We were able to unambiguously place in the electron-density map 14 transmembrane helices (named TM1-TM14), two C-terminal cytosolic STAS domains, and two short cytosolic N-terminal regions.

The structure of prestin is strikingly similar to that of Slc26a9, a representative Slc26 family member, whose structure also has been solved by cryo-electron microscopy (Walter et al., 2019; Chi et al., 2020). Like in Slc26a9, we have found that helices TM1-TM7 and TM8-TM14 are related by a pseudo-C2 symmetry axis which is parallel to the membrane. When compared to the available cryo-EM structures of SLC26a9, our prestin model suggests that it represents a conformation which is closer to the "intermediate" conformation of mouse Slc26a9 (PDB ID,

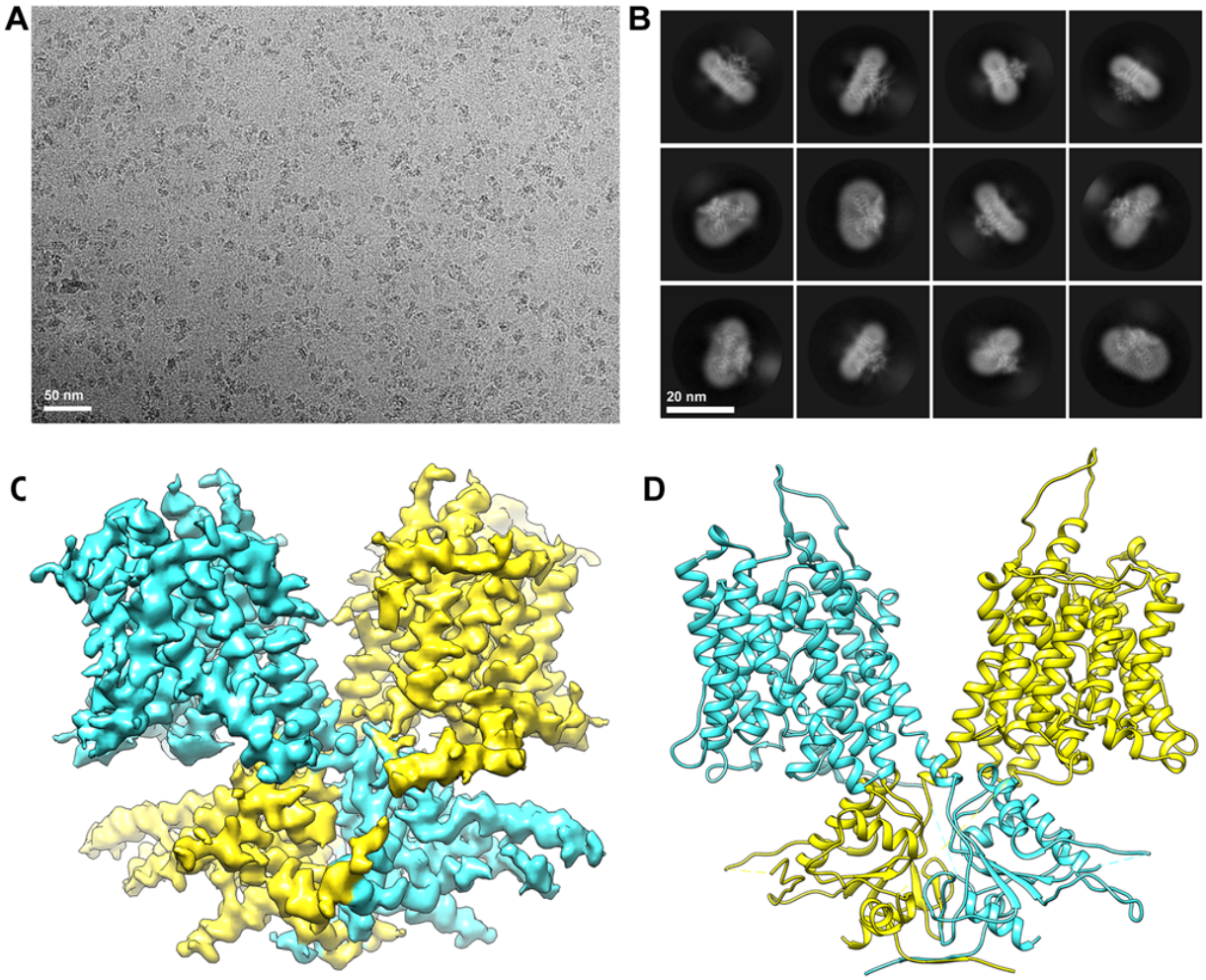

Figure 1. Cryo-EM imaging and the architecture of SLC26a5 (prestin). (**A**) Representative cryo-EM micrograph; (**B**) Selected reference -free 2D class averages; (**C**) Cryo-EM density map of prestin with the density corresponding to the two prestin subunits colored in yellow and cyan respectively. (**D**) Molecular model of prestin based on the cryo-EM density.

6RTF) (C_{alpha} root mean square deviation: 2.985 Å overall) rather than the "inward-open" conformation of mouse Slc26a9 (PDB ID, 6RTC) (C_{alpha} root mean square deviation: 4.25 Å overall). Of note, the solved "inward-open" conformations of human SLC26A9 (PDB ID, 7CH1) and mouse Slc26a9 (PDB ID, 6RTC) are essentially identical , with only very subtle changes. Notably, in the cryo-EM density map of full-length prestin, the IVS loop (variable or intervening sequence) appears to be more interpretable, showing more electron density to build in, when comparing with the equivalent region in the cryo-EM density map of full-length human SLC26A9 (Walter et al., 2019; Chi et al., 2020)

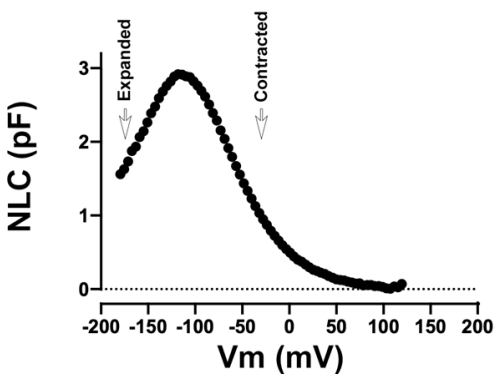

Figure 2. Prestin predominantly resides in the contracted state at 0 mV. Average NLC (n=10), 48 hours after induction of our inducible prestin cell line. Recordings were done in the presence of 140 mM intracellular Cl^-. NLC fitted parameters were Q_{max} = 0.432; z = 0.68; V_h =-114 mV. NLC peaks at V_h.

Functional implications of prestin's structure

We infer that the structure of prestin that we obtained is in the contracted state. Membrane depolarization from a negative resting voltage shifts prestin from an expanded to contracted state, evoking OHC shortening (Ashmore, 1990; Santos-Sacchi, 1991); furthermore, increases in intracellular Cl^- ion concentration cause a hyperpolarizing shift in V_h, the voltage where, based on 2-state models, prestin is equally distributed between compact and expanded states (Oliver et al., 2001; Rybalchenko and Santos-Sacchi, 2003b; Rybalchenko and Santos-Sacchi, 2003a). Our cell line from which we purified prestin (Bian et al., 2010) displays V_h values near -110 mV in the presence of 140 mM Cl^- (**Figure 2**). Since the voltage across detergent micelles is effectively 0 mV, prestin must be in a contracted state.

Despite purification in high chloride, we were unable to resolve an electron density corresponding to a chloride ion within prestin. A similar observation was made with all three structures of Slc26a9 (Walter et al., 2019; Chi et al., 2020), and in prestin's case may be due to its relatively poor Cl^- binding affinity (Oliver et al., 2001; Song and Santos-Sacchi, 2010). Nevertheless, prestin presents the canonical anion binding site features identified in other structurally solved family members where substrates are resolved. The binding site is between TM3 and TM10 and the beta sheets preceding these. Many of the residues important for coordinating substrate binding in those proteins, including S398, F137, and R399, are preserved in similar positions in prestin. Furthermore, with the exception of T127 in Slc26a9 (which is a proline P136 in prestin) other residues important for coordinating water molecules for substrate interactions are also preserved in prestin (Q94, Q97, F101). Although it has been speculated that

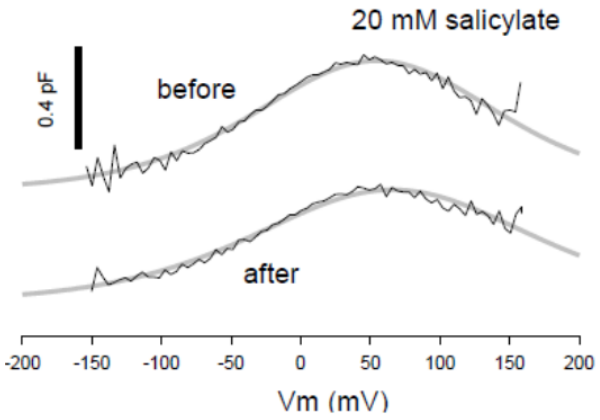

Figure 3. The S398E mutation in prestin preserves NLC after application of 20mM salicylate. Controls shows full block of NLC. The average unitary gating charge (z) in these mutants (0.69e +/- 0.03 SEM, n =7) was similar to that of CHO cells expressing prestin-YFP (0.73e +/- 0.14 SEM, n=10, P>0.05).

Cl^- acts as an extrinsic voltage sensor (Oliver et al., 2001), this speculation has never been confirmed; instead, anions have been shown to foster allosteric-like modulation of prestin activity and kinetics, with anion substitute valence showing no correlation with magnitude of prestin's unitary charge (Rybalchenko and Santos-Sacchi, 2003a; Rybalchenko and Santos-Sacchi, 2003b, 2008; Song and Santos-Sacchi, 2010, 2013; Santos-Sacchi and Song, 2016). It is well known that salicylate blocks NLC and electromotility (Tunstall et al., 1995; Kakehata and Santos-Sacchi, 1996), possibly by competitively displacing Cl^-(Oliver et al., 2001). Here we show that mutation of S398 in the structurally identified anion binding pocket of prestin to a negatively charged glutamate residue results in a protein that is insensitive to salicylate yet retains normal NLC (**Figure 3**). This observation is further evidence against Cl^- acting as an extrinsic voltage sensor. We see similar effects with R399. Indeed, recently, Oliver (Gorbunov et al., 2018) reported on S396E which shows insensitivity to salicylate as proof refuting his original extrinsic voltage sensor hypothesis. They also previously observed salicylate insensitivity with R399S (Gorbunov et al., 2014). Another mutation within the anion binding pocket of prestin, F127 to alanine, resulted in a loss of NLC or a far-right shift in its voltage sensitivity that made its detection impossible (Bai et al., 2017), although this mutation also had detectable SCN currents that were displaced in a depolarizing direction. These mutations of prestin's Cl^- binding site, besides refuting the extrinsic voltage sensor hypothesis, also make implausible any associated transport-like requirements for voltage-driven electromotility.

The marked structural similarity between prestin and Slc26a9 may provide insight into prestin's electromechanical behavior. In prestin, several charged residues have been shown to affect the size of unitary gating charge and thus contribute to voltage sensing (Bai et al., 2009b).

Of those twelve residues, 9 are conserved in Slc26a9. We transiently expressed Slc26a9 in CHO cells but were unable to find NLC or gating currents that are robustly observed in transiently transfected prestin CHO cells (**Figure 4 A,B**). Slc26a9 surface expression in transfected cells was successful as demonstrated by enhanced currents in the presence of extracellular SCN^- (**Figure 4 C,D**) and visualization of fluorescence on the surface of these cells expressing Slc26a9 with YFP tagged to its C-terminus (**Figure 4A, insert**). Thus, despite marked structural similarities to prestin, Slc26a9 does not mimic prestin's electromechanical behavior.

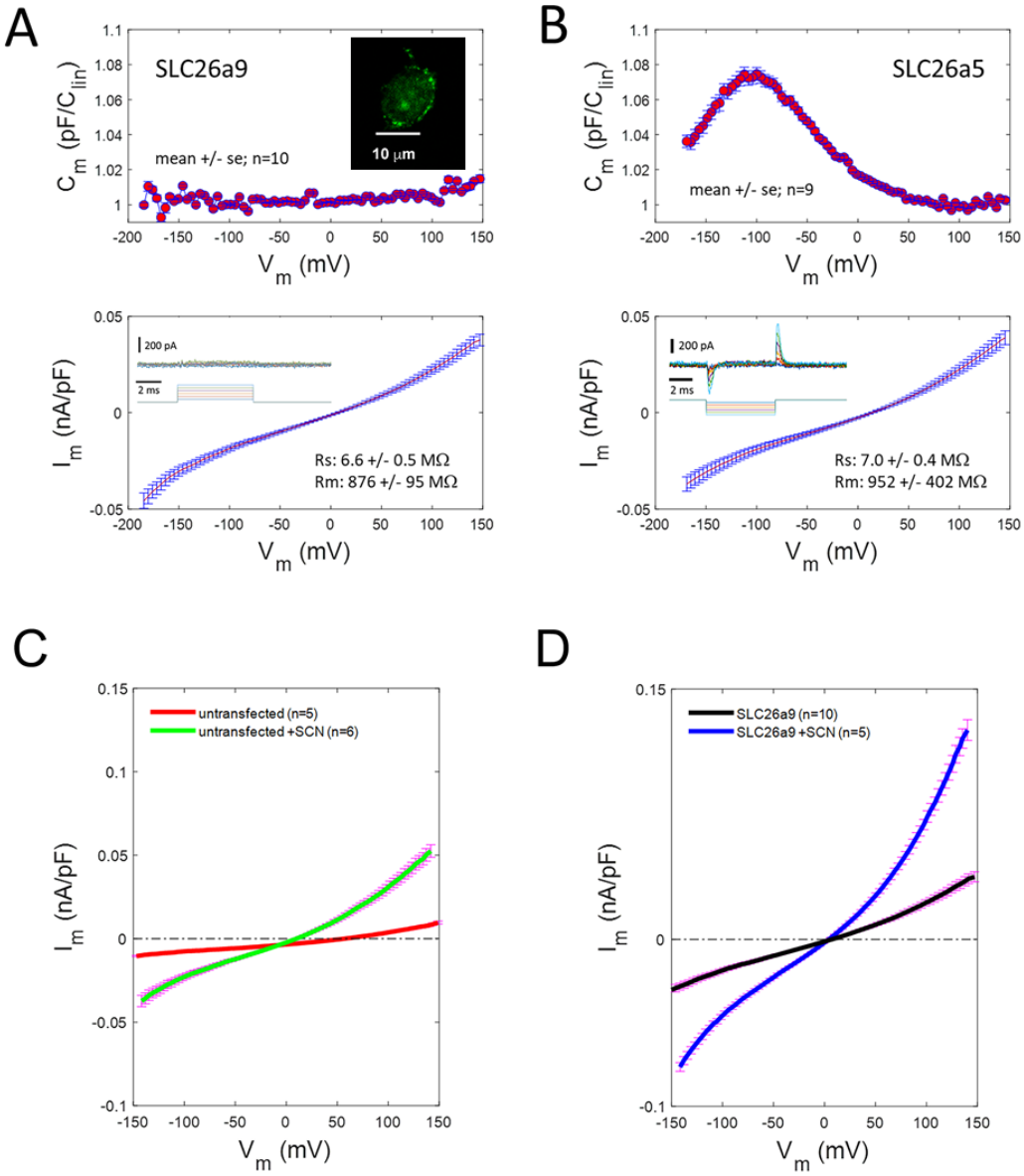

Figure 4. (**A**) *Top panel*: Capacitance of CHO cells transiently infected with Slc26a9, scaled to linear capacitance near -100 mV. Measured with dual-sine voltage superimposed on a voltage ramp from -175 to + 150 mV. A very slight increase in C_m occurs at +150 mV possibly indicating an extremely right-shifted NLC. *Insert*: Confocal image of CHO cell transfected with Slc26a9-YFP that is expressed on the membrane. The scale bar is 10 microns. *Bottom panel:* Ramp induced currents simultaneously measured with membrane capacitance, also scaled to linear capacitance. *Insert*: top traces show very small nonlinear currents extracted with P/-5 protocol, subtraction holding potential set to -50 mV. Voltage protocol shown below traces. (**B**) *Top panel*: Capacitance of CHO cells transiently infected with Slc26a5, scaled to linear capacitance near +100 mV. Measured with dual-sine voltage superimposed on a voltage ramp from -175 to + 150 mV. A prominent increase in C_m occurs at -110 mV, typical of prestin NLC. *Bottom panel:* Ramp induced currents simultaneously measured with membrane capacitance, also scaled to linear capacitance. *Insert*: top traces show large nonlinear displacement currents extracted with P/-5 protocol, subtraction holding potential set to +50 mV. Voltage protocol shown below traces. (**C**) Effect of SCN^- on the magnitude of ramp induced current in un-transfected CHO cells. A slight increase in current is observed with SCN^-. (**D**) In Slc26a9 transfected cells, larger currents are observed without and with SCN^-, indicating successful delivery of the construct to the membrane.

Discussion

We found that the overall molecular architecture of prestin is strikingly similar to the previously reported cryo-EM structures of full-length human SLC26A9 (Walter et al., 2019; Chi et al., 2020) and of a shorter version of mouse Slc26a9 protein (Walter et al., 2019; Chi et al., 2020), whose functions are to facilitate the transport of anions. Slc26A9 allows entry of the substrates (anions) from the cytoplasm through the so called "inward-open" conformation, which shows an opening between the "core" and the "gate" domains as described in the solved cryo-EM structures (Walter et al., 2019; Chi et al., 2020). Intriguingly, we have found based on root mean square deviations over C_{alpha} atoms, between the cryo-EM structure of prestin and the solved cryo-EM structures of Slc26a9, that the membrane spanning portion of prestin does not conform to the "inward-open" conformation of Slc26a9. Rather, prestin has a more compact conformation, closer to the "inward-open/intermediate" conformation of Slc26a9 solved by cryo-EM (PDB ID, 6RTF), which shows the cytosol-exposed space between the "core" and the "gate" domains to be tighter. We reason that the prestin conformation solved by cryo-EM represents the contracted state of the protein at 0 mV.

Finally, we have compared our prestin cryo-EM structure to the predicted structure by the Alpha-Fold algorithm and find that despite overall similar topology, the pair-wise C_{alpha} root mean square deviation calculated over the number of residues resolved in the cryo-EM structure is 15.712 Å.

Key functional implications of prestin structure

Our structural data allow us to answer key questions concerning prestin's molecular behavior. For example, given actual anion binding pocket structural features (not assumed from other family members) we can unequivocally assign relevance to prior and present mutational perturbations. Thus, we present data here that Cl^- does not function as prestin's extrinsic voltage sensor, evidenced by the loss of anion sensitivity with structurally driven mutations in the anion binding site. Instead, prestin possesses charged residues important for voltage sensing, akin to

other voltage sensing membrane proteins (Bezanilla, 2008; Bai et al., 2009a). The distribution of twelve charged residues that sense voltage in prestin has important implications. Seven of the 12 residues are located in the dimerization domain in TMs 5,6 and 12 that are modelled to move minimally in the elevator model (Bai et al., 2009b; Drew and Boudker, 2016; Ficici et al., 2017). Notably, all but one of the 12 residues lie in the intracellular halves of the TM domains or in the intracellular loop connecting these TM domains. In contrast, all but one of the five charged residues that have no effect on voltage sensing lie close to the extracellular halves of the TM domain or in the loops connecting these TM domains. This includes a charged residue in TM 3 (R150), that is modeled to move significantly in the transporter cycle (Bai et al., 2009b; Drew and Boudker, 2016; Ficici et al., 2017). Together, these data suggest that contrary to functional expectations based solely on structural similarity between prestin and Slc26a9, electromechanical behavior in prestin is fundamentally different to transporter movements and concentrated in proximity to the intracellular opening.

We have determined that prestin is dimeric, although earlier reports asserted that prestin functions as a tetramer (Wang et al., 2010; Hallworth and Nichols, 2012). In Slc26a9, three features were identified as important for dimerization, and likely are pertinent for prestin considering the proteins' remarkable similarity. These include membrane interactions between individual protomers exemplified by the valine zipper in TM14, interactions between the C terminal STAS domain of one protomer and the TM domains of the other and an antiparallel beta strand between the N terminus of both protomers. Prestin shows each of these same interactions with the valine zipper being replaced by leucine and isoleucine residues. The anti-parallel beta sheet between the N terminal residues 11-21 of each protomer in prestin is likely critical for dimerization. Indeed, sequential deletion of these residues resulted in progressive loss of NLC, and loss of FRET signal confirming loss of dimerization (Navaratnam et al., 2005). These data also argue that dimerization is critical for NLC, just as dimerization is important for transporter function in UraA (Lu et al., 2011; Yu et al., 2017).

The C-terminus of prestin cryo-EM structure is similar to the previously determined X-ray crystal structure of the C-terminal STAS domain (PDB ID,3LLO) lacking the unstructured loop (Pasqualetto et al., 2010). Thus, we see an identical core of five beta sheets surrounded by 5

alpha helices. The root mean square deviation (rmsd) between prestin's C-terminal domain solved by cryo-EM and prestin's C-terminal domain solved by X-ray crystallography (PDB ID,3LLO) is 0.853 Å over 105 C_{alpha} atoms. The many interpretations made by the Battistutta group are likely to therefore apply, including confirmation in our structure of the orientation of the STAS domain to the transmembrane domain, and the importance of the alpha 5 helix in stabilizing the core beta sheets suggested by truncation experiments (Navaratnam et al., 2005; Zheng et al., 2005). A significant difference was in the first alpha helix that is parallel to the second alpha helix as in bacterial ASA (anti-sigma factor antagonistic) proteins (Aravind and Koonin, 2000), and deviated by a 30^0 angle in the crystal structure (Pasqualetto et al., 2010). This is likely due to the unstructured loop at the end of the first alpha helix that was lacking in the crystal structure.

Summary

OHC electromotility was discovered in 1985 (Brownell et al., 1985), and 15 years later prestin was identified as the protein responsible for the OHC's unique role in cochlear amplification (Zheng et al., 2000). During the intervening years enormous detail into the protein's function has been obtained, see (Santos-Sacchi et al., 2017). More recent homology modelling of prestin (Gorbunov et al., 2014), based on presumed similarity to other family members, and confirmed in our structural data, has moved us closer to understanding prestin's electromechanical behavior. Indeed, the cryo-EM solution we provide here will permit us to rigorously interpret past studies and design new experiments to more fully understand prestin's role in mammalian hearing. Given the remarkable similarity of prestin structure revealed in this present study to that of the inside open/ intermediate state of Slc26a9, key questions remain as to why the two proteins differ in their function. Current functional observations on prestin may have already identified key differences, for example, the observed negative cooperativity among the densely packed proteins interacting through membrane lipids (10,000/μm^2 in OHCs) (Zhai et al., 2020), and subplasmalemmal cytoskeletal interactions with prestin (Bai et al., 2010). Though key, prestin likely is a partner in the machinery that boosts our hearing abilities. Imperative in the overall effort to understand prestin is the need for alternative structures of prestin and other family members.

Materials and Methods

Prestin Expression and Purification

The full-length prestin from gerbil (*Meriones unguiculatus, Genbank accession number* AF230376) was purified from a tetracycline inducible stable HEK 293 cell line (Bian et al., 2010) . In establishing this cell line (16C), full length gerbil prestin cDNA (a gift from J. Zheng and P. Dallos) tagged at its C-terminus with enhanced yellow fluorescent protein (EYFP) was inserted into the multiple cloning site of pcDNA4/TO/*myc*-HisC that allowed purification using Ni affinity.

Cells were grown in DMEM media supplemented with 1 mM L-glutamine, 100 U ml^{-1} penicillin/streptomycin, 10% FBS and 1 mM sodium pyruvate. 4 µg/ml of blasticidin and 130 µg/ml of zeocin were supplemented in the growth media to maintain prestin expression. Cells were harvested 48 hours after tetracycline (1 µg/ml) was added to the cell growth medium to induce prestin expression.

Cell pellets from 20 T175 Flasks were harvested by centrifugation at 1,000g for 10 minutes, washed with PBS, then resuspended in 5ml of resuspension buffer (25 mM HEPES, pH 7.4, 200 mM NaCl, 5% glycerol, 2mM $CaCl_2$, 10 µg/ml^{-1} DNase I and 1 protease inhibitors (cOmplete EDTA-free, Roche) for each gram of pellet. 2% (wt/vol final concentration) digitonin (Anatrace) powder was directly dissolved in the cell resuspension, and the mixture was incubated for 1.5 hr under gentle agitation (rocking) at 4^0C. Insoluble material was removed by centrifugation at 160,000 g for 50 minutes (Beckman L90-XP ultracentrifuge with a 50.2 Ti rotor). The supernatant was passed through a 0.45 µm filter. 10 mM imidazole (final concentration) and 1 ml Ni-NTA resin (Qiagen) pre-washed in 25mM Hepes, pH 7.4, 200 mM NaCl, 5% glycerol, 2mM $CaCl_2$, 0.02% GDN (synthetic digitonin substitute glyco-diosgenin, Antrace) were added to the filtered supernatant and incubated with end over end rocking agitation at 4 ^{0}C for 2 hours. The resin was collected using a bench Eppendorf microcentrifuge and washed sequentially with high salt buffer Buffer A (25 mM HEPES, pH 7.4, 500 mM NaCl, 5% glycerol, and 0.02% GDN) and 25ml Buffer B (25 mM HEPES, pH 7.4, 200 mM NaCl, 10 mM imidazole, 5% glycerol, and 0.02% GDN). The protein was eluted in 1.5ml Buffer C (25 mM HEPES, pH 7.4, 200 mM NaCl, 250 mM imidazole, 5% glycerol, and 0.02% GDN). The 1.5 ml eluted protein was concentrated to 500 µl,

passed through a 0.22 µm filter and loaded onto a FSEC column (Superdex 200 Increase 10/300 GL column, on a Shimadzu FPLC system) equilibrated with gel-filtration buffer (10 mM HEPES, 200 mM NaCl, 0.02% GDN, pH 7.4). Two 0.5 ml fractions corresponding to the fluorescent (excitation 488 nm, emission 535 nm) peak and A280 peak were collected and concentrated using an Amicon Ultra centrifugal filter with a molecular weight cutoff 100 KDa and used for freezing grids.

Sample Preparation and Data Acquisition

An aliquot of four microliters of purified prestin (at a concentration of approximately 2 mg/ml) was applied to glow-discharged Quantifoil holey carbon grids (Gold R2/1; 200 mesh) overlaid with an additional 2-nm carbon layer (Electron Microscopy Sciences). The grids were blotted for 3-5 s and plunge-frozen in liquid ethane using a Vitrobot Mark IV (FEI) instrument with the chamber maintained at 10^0C and 100% humidity.

Cryo-EM micrograph movies were recorded using the SerialEM software on a Titan Krios G2 transmission electron microscope (Thermo Fischer/FEI) operated at a voltage of 300 kV and equipped with a K3 Summit direct electron detector (Gatan, Pleasanton, CA). A quantum energy filter with a 20 eV slit width (Gatan) was used to remove the inelastically scattered electrons. In total 4,680 dose-fractionated super-resolution movies with 36 images per stack were recorded. The cryo-EM movies were recorded with a defocus varied from –1.15 to –2.15 µm at a nominal magnification of 81,000x (corresponding to 0.534 Å per pixel). The counting rate was 17.5 e^-/physical pix/s. The total exposure time was 3.6 s per exposure with a total dose of ~ 54 $e^-/Å^2$.

Data Processing

Movies frames were gain-normalized and motion-corrected using MotionCor2 (as implemented in Relion 3.1 (Zivanov et al., 2018)) with a binning factor of 2 and dividing micrographs into 4x4 patches. The dose-weighted, motion corrected micrographs (the sum of 36 movie frames) were used for all image processing steps except for defocus determination. The contrast transfer function (CTF) calculation was perform with CTFFIND4.1 (as implemented in Relion3.1) on movie sums which were motion-corrected but not dose-weighted. About 3,000

particles were manually picked and subjected to 2D reference-free classification in Relion 3.1 (Zivanov et al., 2018).

Classes showing good signal (representing ~1,100 particles) were chosen as references for automated particle picking in Relion 3.1, yielding a data set of ~1,377,109 particles. Several rounds of 2D and 3D classification (carried out without application of symmetry) were used to remove unsuitable particles, leaving 122,754 particles that were used for structural determination with imposed C2 symmetry in Relion 3.1. Bayesian polishing (Zivanov et al., 2018), followed by per-particle contrast transfer function (CTF) refinement (as implemented in Relion 3.1), 3D auto-refinement, micelle density subtraction and post-processing generated a map which had an estimated resolution of ~ 4 Å according to the Fourier shell correlation (FSC) =0.143 criterion.

Model Building

The SLC26a9 cryo-EM intermediate structure (PDB ID, 6RT which is a poly-alanine trace) was rigid-body docked into the prestin cryo-EM map and fitted using Chimera (Pettersen et al., 2004). Next, the poly-alanine trace was refined in COOT (Emsley et al., 2010) by manually going through the entire protomer chains. Sequence assignment was guided mainly by bulky residues such as Phe, Tyr, Trp, and Arg, and secondary structure predictions. Side chains in areas of the map with insufficient density were left as alanine. The model was refined through several rounds of model building in COOT and real-space refinement in PHENIX (Adams et al., 2010) with secondary structure and geometry restraints.

Electrophysiological recording

Recordings were made of transiently transfected CHO (or HEK cells 48 hours after tetracycline induction) using a whole-cell configuration at room temperature using an Axon 200B amplifier (Molecular Devices, Sunnyvale, CA), as described previously. Cells were recorded 48–72 h after tetracycline induction or transfection to allow for stable measurement of current and NLC. The standard bath solution components were (in mM): 100 NaCl (TEA)-Cl 20, CsCl 20, $CoCl_2$ 2, $MgCl_2$ 2, Hepes 5, pH 7.2. In addition, 20mM NaSCN was substituted for current

recordings with cells transiently transfected with Slc26a9. The pipette solution contained (in mM): NaCl 100, CsCl 20, EGTA 5, $MgCl_2$ 2, Hepes 10, pH 7.2. Osmolarity was adjusted to 300 ± 2 mOsm with dextrose. After whole cell configuration was achieved in extracellular NaCl a ramp protocol recorded to confirm baseline NLC and currents. Pipettes had resistances of 3-5 MΩ. Gigohm seals were made and stray capacitance was balanced out with amplifier circuitry prior to establishing whole-cell conditions. A Nikon Eclipse E600-FN microscope with 40× water immersion lens was used to observe cells during voltage clamp. Data were low pass filtered at 10 kHz and digitized at 100 kHz with a Digidata 1320A.

Command delivery and data collections were carried out with a Windows-based whole-cell voltage clamp program, jClamp (Scisoft, East Haven, CT), using a Digidata 1322A (Axon Instruments). A continuous high-resolution 2-sine voltage command was used, cell capacitance and current being extracted synchronously. Capacitance data were fitted to the first derivative of a two-state Boltzmann function:

$$C_m = Q_{max} \frac{ze}{kT} \frac{b}{(1+b)^2} + C_{lin} \qquad (1)$$

where

$$b = \exp\left(-\frac{ze\,(V_m - V_{vh})}{kT}\right) \qquad (2)$$

Q_{max} is the maximum nonlinear charge transfer, V_h the voltage at peak capacitance or half-maximal nonlinear charge transfer, V_m the membrane potential, C_{lin} linear capacitance, z the unitary charge (a metric of voltage sensitivity), e the electron charge, k the Boltzmann constant, and T the absolute temperature. Q_{sp} the specific charge density, is the total charge moved (Q_{max}) normalized to linear capacitance. Voltages were corrected for series resistance voltage drop. Separately, in specific experiments gating currents were also determined using voltage steps (50 ms duration) from −100 mV to 150 mV, with 20 mV step increments. Where anions were substituted, local perfusion of the cells were estimated to give rise to small junctional potentials (JPCalc function in pClamp). Since these numbers were small no corrections were made to the IV plots. For solution perfusion experiments we used a QMM perfusion system (ALA Scientific,

Instruments, Westbury, NY). The manifold's output tip was 200 µm placed 1 mm from the cell, and the flow rate increased by an applied pressure of approximately 20 kPa. Statistical analysis was done with SAS software (SAS Institute Inc, NC).

References

Adams PD, Afonine PV, Bunkoczi G, Chen VB, Davis IW, Echols N, Headd JJ, Hung LW, Kapral GJ, Grosse-Kunstleve RW, McCoy AJ, Moriarty NW, Oeffner R, Read RJ, Richardson DC, Richardson JS, Terwilliger TC, Zwart PH (2010) PHENIX: a comprehensive Python-based system for macromolecular structure solution. Acta Crystallogr D Biol Crystallogr 66:213-221.

Aravind L, Koonin EV (2000) The STAS domain - a link between anion transporters and antisigma-factor antagonists. Curr Biol 10:R53-55.

Ashmore J (2005) Prestin is an electrogenic anion transporter. 42ndWorkshop on Inner Ear Biology Sept.:138.

Ashmore JF (1990) Forward and reverse transduction in the mammalian cochlea. Neurosci Res Suppl 12:S39-S50.

Bai J-P, Surguchev A, Montoya S, Aronson PS, Santos-Sacchi J, Navaratnam D (2009a) Prestin's Anion Transport and Voltage-Sensing Capabilities Are Independent. Biophys J 96:3179-3186.

Bai JP, Surguchev A, Montoya S, Aronson PS, Santos-Sacchi J, Navaratnam D (2009b) Prestin's anion transport and voltage-sensing capabilities are independent. Biophys J 96:3179-3186.

Bai JP, Surguchev A, Ogando Y, Song L, Bian S, Santos-Sacchi J, Navaratnam D (2010) Prestin surface expression and activity are augmented by interaction with MAP1S, a microtubule-associated protein. JBiolChem 285:20834-20843.

Bai JP, Moeini-Naghani I, Zhong S, Li FY, Bian S, Sigworth FJ, Santos-Sacchi J, Navaratnam D (2017) Current carried by the Slc26 family member prestin does not flow through the transporter pathway. Sci Rep 7:46619.

Bezanilla F (2008) How membrane proteins sense voltage. NatRevMolCell Biol 9:323-332.

Bian S, Koo BW, Kelleher S, Santos-Sacchi J, Navaratnam DS (2010) A highly expressing Tet-inducible cell line recapitulates in situ developmental changes in prestin's Boltzmann characteristics and reveals early maturational events. AmJPhysiol Cell Physiol 299:C828-C835.

Brownell WE, Bader CR, Bertrand D, de Ribaupierre Y (1985) Evoked mechanical responses of isolated cochlear outer hair cells. Science 227:194-196.

Chang YN, Geertsma ER (2017) The novel class of seven transmembrane segment inverted repeat carriers. Biol Chem 398:165-174.

Chang YN, Jaumann EA, Reichel K, Hartmann J, Oliver D, Hummer G, Joseph B, Geertsma ER (2019) Structural basis for functional interactions in dimers of SLC26 transporters. Nat Commun 10:2032.

Chi X, Jin X, Chen Y, Lu X, Tu X, Li X, Zhang Y, Lei J, Huang J, Huang Z, Zhou Q, Pan X (2020) Structural insights into the gating mechanism of human SLC26A9 mediated by its C-terminal sequence. Cell Discov 6:55.

Dallos P, Wu X, Cheatham MA, Gao J, Zheng J, Anderson CT, Jia S, Wang X, Cheng WH, Sengupta S, He DZ, Zuo J (2008) Prestin-based outer hair cell motility is necessary for mammalian cochlear amplification. Neuron 58:333-339.

Drew D, Boudker O (2016) Shared Molecular Mechanisms of Membrane Transporters. Annu Rev Biochem 85:543-572.

Emsley P, Lohkamp B, Scott WG, Cowtan K (2010) Features and development of Coot. Acta Crystallogr D Biol Crystallogr 66:486-501.

Ficici E, Faraldo-Gomez JD, Jennings ML, Forrest LR (2017) Asymmetry of inverted-topology repeats in the AE1 anion exchanger suggests an elevator-like mechanism. J Gen Physiol 149:1149-1164.

Gale JE, Ashmore JF (1994) Charge displacement induced by rapid stretch in the basolateral membrane of the guinea-pig outer hair cell. Proc R Soc Lond B Biol Sci 255:243-249.

Gorbunov D, Hartmann J, Renigunta V, Oliver D (2018) A glutamate scan identifies an electrostatic switch for prestin activity. Midwinter Meeting Abstracts of the Associatio for Research in Otolaryngology.

Gorbunov D, Sturlese M, Nies F, Kluge M, Bellanda M, Battistutta R, Oliver D (2014) Molecular architecture and the structural basis for anion interaction in prestin and SLC26 transporters. Nat Commun 5:3622.

Hallworth R, Nichols MG (2012) Prestin in HEK cells is an obligate tetramer. J Neurophysiol 107:5-11.

Iwasa KH (1993) Effect of stress on the membrane capacitance of the auditory outer hair cell. Biophys J 65:492-498.

Kakehata S, Santos-Sacchi J (1995) Membrane tension directly shifts voltage dependence of outer hair cell motility and associated gating charge. Biophys J 68:2190-2197.

Kakehata S, Santos-Sacchi J (1996) Effects of salicylate and lanthanides on outer hair cell motility and associated gating charge. J Neurosci 16:4881-4889.

Kuwabara MF, Wasano K, Takahashi S, Bodner J, Komori T, Uemura S, Zheng J, Shima T, Homma K (2018) The extracellular loop of pendrin and prestin modulates their voltage-sensing property. J Biol Chem 293:9970-9980.

Lu F, Li S, Jiang Y, Jiang J, Fan H, Lu G, Deng D, Dang S, Zhang X, Wang J, Yan N (2011) Structure and mechanism of the uracil transporter UraA. Nature 472:243-246.

Ludwig J, Oliver D, Frank G, Klocker N, Gummer AW, Fakler B (2001) Reciprocal electromechanical properties of rat prestin: The motor molecule from rat outer hair cells. Proc Natl Acad Sci U S A 98:4178-4183.

Navaratnam D, Bai JP, Samaranayake H, Santos-Sacchi J (2005) N-terminal-mediated homomultimerization of prestin, the outer hair cell motor protein. Biophys J 89:3345-3352.

Oliver D, He DZ, Klocker N, Ludwig J, Schulte U, Waldegger S, Ruppersberg JP, Dallos P, Fakler B (2001) Intracellular anions as the voltage sensor of prestin, the outer hair cell motor protein. Science 292:2340-2343.

Pasqualetto E, Aiello R, Gesiot L, Bonetto G, Bellanda M, Battistutta R (2010) Structure of the cytosolic portion of the motor protein prestin and functional role of the STAS domain in SLC26/SulP anion transporters. J Mol Biol 400:448-462.

Pettersen EF, Goddard TD, Huang CC, Couch GS, Greenblatt DM, Meng EC, Ferrin TE (2004) UCSF Chimera--a visualization system for exploratory research and analysis. J Comput Chem 25:1605-1612.

Rybalchenko V, Santos-Sacchi J (2003a) Allosteric modulation of the outer hair cell motor protein prestin by chloride. In: Biophysics of the Cochlea: From Molecules to Models (Gummer A, ed), pp 116-126. Singapore: World Scientific Publishing.

Rybalchenko V, Santos-Sacchi J (2003b) Cl- flux through a non-selective, stretch-sensitive conductance influences the outer hair cell motor of the guinea-pig. J Physiol 547:873-891.

Rybalchenko V, Santos-Sacchi J (2008) Anion control of voltage sensing by the motor protein prestin in outer hair cells. Biophys J 95:4439-4447.

Santos-Sacchi J (1991) Reversible inhibition of voltage-dependent outer hair cell motility and capacitance. J Neurosci 11:3096-3110.

Santos-Sacchi J, Song L (2016) Chloride anions regulate kinetics but not voltage-sensor Qmax of the solute carrier SLC26a5. Biophys J 110:1-11.

Santos-Sacchi J, Tan W (2020) Complex nonlinear capacitance in outer hair cell macro-patches: effects of membrane tension. Sci Rep 10:6222.

Santos-Sacchi J, Shen W, Zheng J, Dallos P (2001) Effects of membrane potential and tension on prestin, the outer hair cell lateral membrane motor protein. J Physiol 531:661-666.

Santos-Sacchi J, Song L, Zheng JF, Nuttall AL (2006) Control of mammalian cochlear amplification by chloride anions. J Neurosci 26:3992-3998.

Santos-Sacchi J, Navaratnam D, Raphael R, Oliver D (2017) The Cochlea Chapter 5: Prestin - molecular mechanisms underlying outer hair cell electromotility. Springer Handbook Of Auditory Research. New York: Springer.

Song L, Santos-Sacchi J (2010) Conformational state-dependent anion binding in prestin: evidence for allosteric modulation. Biophys J 98:371-376.

Song L, Santos-Sacchi J (2013) Disparities in voltage-sensor charge and electromotility imply slow chloride-driven state transitions in the solute carrier SLC26a5. Proc Natl Acad Sci U S A.

Tang J, Pecka JL, Tan X, Beisel KW, He DZ (2011) Engineered pendrin protein, an anion transporter and molecular motor. JBiolChem 286:31014-31021.

Tunstall MJ, Gale JE, Ashmore JF (1995) Action of salicylate on membrane capacitance of outer hair cells from the guinea-pig cochlea. J Physiol 485 (Pt 3):739-752.

Walter JD, Sawicka M, Dutzler R (2019) Cryo-EM structures and functional characterization of murine Slc26a9 reveal mechanism of uncoupled chloride transport. Elife 8.

Wang X, Yang S, Jia S, He DZ (2010) Prestin forms oligomer with four mechanically independent subunits. Brain Res 1333:28-35.

Yu X, Yang G, Yan C, Baylon JL, Jiang J, Fan H, Lu G, Hasegawa K, Okumura H, Wang T, Tajkhorshid E, Li S, Yan N (2017) Dimeric structure of the uracil:proton symporter UraA provides mechanistic insights into the SLC4/23/26 transporters. Cell Res 27:1020-1033.

Zhai F, Song L, Bai JP, Dai C, Navaratnam D, Santos-Sacchi J (2020) Maturation of Voltage-induced Shifts in SLC26a5 (Prestin) Operating Point during Trafficking and Membrane Insertion. Neuroscience 431:128-133.

Zheng J, Shen W, He DZ, Long KB, Madison LD, Dallos P (2000) Prestin is the motor protein of cochlear outer hair cells. Nature 405:149-155.

Zheng J, Du GG, Matsuda K, Orem A, Aguinaga S, Deak L, Navarrete E, Madison LD, Dallos P (2005) The C-terminus of prestin influences nonlinear capacitance and plasma membrane targeting. J Cell Sci 118:2987-2996.

Zivanov J, Nakane T, Forsberg BO, Kimanius D, Hagen WJ, Lindahl E, Scheres SH (2018) New tools for automated high-resolution cryo-EM structure determination in RELION-3. Elife 7.

Supplemental Figures

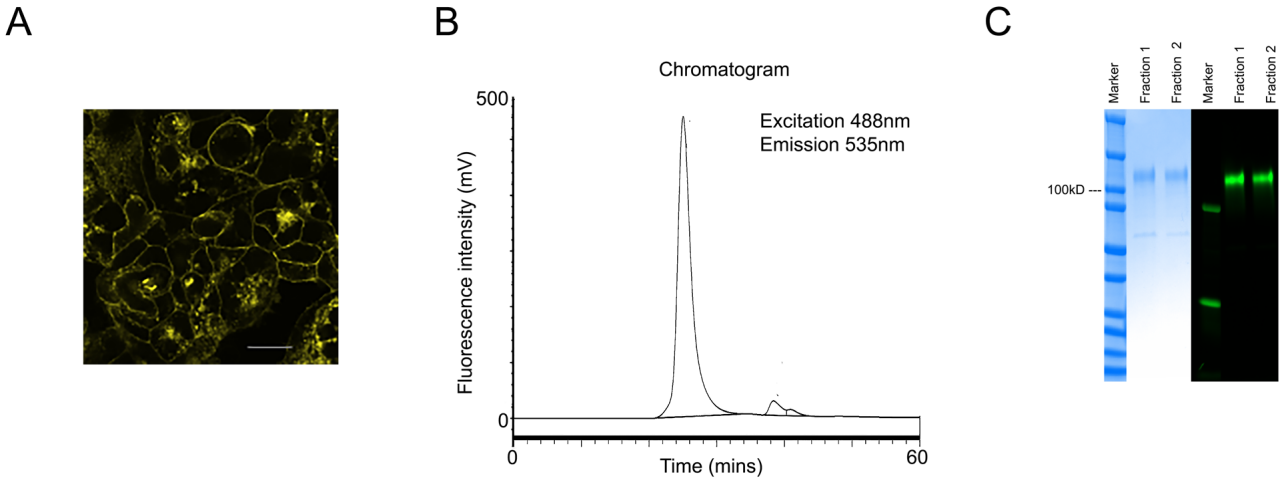

Supplementary Figure 1. (**A)**. The figure shows a fluorescence image of HEK 293 cells 48 hours after tetracycline induction with prestin YFP expressed in the plasma membrane of cells. Scale bar is 10 microns. (**B**) Fluorescence Size Exclusion Chromatogram (FSEC) of purified prestin YFP injected into a Superdex 200 Increase 10/300 GL Column . Two fractions corresponding to the single monodisperse peak were collected and used for cryo-EM analysis. (**C)**. Coomasie blue staining (left three lanes) and fluorescence in gel imaging of the two fractions obtained from FSEC confirmed the presence of purified prestin-YFP (~110 kDa). The position of the 100kDa molecular weight marker is indicated.

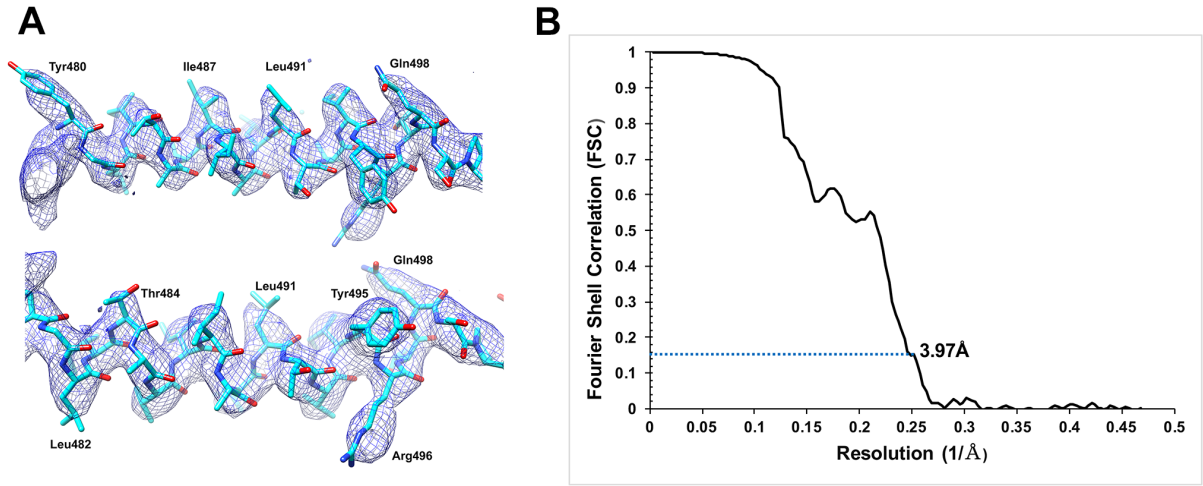

Supplementary Figure 2. Global resolution and the fit of the model to the cryo-EM density. (A) Representative density around the region Tyr480-Gln498. (B) Fourier shell correlation (FSC) curve with indicated resolution at FSC=0.143.